EarthObsNet: A Comprehensive Benchmark Dataset for Data-Driven Earth Observation Image Synthesis

Zhouyayan Li[a,b,*], Yusuf Sermet[b], Ibrahim Demir[a,b,c]

[a] Dept. of Civil and Environmental Engineering, University of Iowa, Iowa City, Iowa, USA
[b] IIHR Hydroscience and Engineering, University of Iowa, Iowa City, Iowa, USA
[c] Dept. of Electrical and Computer Engineering, University of Iowa, Iowa City, Iowa, USA
[*] Corresponding Author, Email: zhouyayan-li@uiowa.edu

Abstract

Remote Sensing imagery serves as an important data source for Earth surface monitoring and surface processes studies. It is highly likely that RS imagery will become more and more indispensable in the future due to its high scalability and compatibility with data-driven models and ever-evolving software and hardware that become increasingly good at processing large datasets. Although its promising future, the usage of Earth surface observation imagery, such as Landsat, Sentinel-2, and Sentinel-1 images, has been largely limited to retrospective studies, where those images serve mainly as documentations of past events. Recently, there are attempts to expand the current usage of RS Earth surface observation images to forward-looking applications to support decision-making and fast response against future natural hazards. Unlike many well-defined and well-studied topics such as change detection and semantic segmentation for which many benchmark datasets are openly available, so far, there are limited public datasets for Earth surface observation image synthesis tasks for fast prototyping and comparison. To close this gap, we introduced a comprehensive dataset containing previous Earth surface observations, precipitation, soil moisture, land cover, Height Above Nearest Drainage (HAND), DEM, and slope collected during the catastrophic 2019 Central US Flooding events that lasted more than two seasons in Mississippi and Missouri River tributaries. We also incorporated reference labels to allow further investigation of the usefulness of the synthesized images in downstream applications, such as flood inundation mapping. We hope to provide an essential dataset for Earth observation image synthesis studies, with the goal of attracting more attention and inspiring more efforts to broaden the usage of Earth surface observation images into forward-looking applications.

Keywords: benchmark dataset; Earth's surface image synthesis; multi-purpose analysis; deep learning; SAR; meteorological and geomorphic input

1. Introduction

Remote Sensing (RS) images, especially Earth's surface observation images, such as Landsat, Sentinel-2, and Sentinel-1 SAR images, are playing an increasingly important role in tasks aimed at monitoring Earth's surface and describing surface phenomena and processes. RS images have the advantage of high spatial and temporal consistency, great scalability, and less manual labor requirements during image collection stages over many traditional and newly emerged ways of data collection (Ali & Ogie, 2017). Those advantages make RS imagery an ideal data source for data-driven methods, especially machine learning (ML) and deep learning (DL) architectures.

However, so far, most of the existing studies utilized RS images, especially those Earth surface observation images, in a retrospective way – reconstructing past events with RS images that captured those events, including flood inundation mapping (Singh & Kansal, 2022), flood susceptibility (Fang et al., 2021; Cikmaz et al., 2023), change detection (Zhang et al., 2020), cloud removal (Xiong et al., 2023), spatiotemporal image fusion (Yang et al., 2021), and so on. Although retrospective studies are valuable in providing insights about and enhancing our understanding of previous events or phenomena, they have limited use in supporting decision making and helping with fast response against future events, as there are no Earth's surface observation images coming before those events for scientists to work on.

Non-stationary processes, as a consequence of anthropogenic activities and climate change, have an increasingly negative impact on the validity of conclusions obtained by analyzing data from past events (Slater et al., 2021). In RS research field, this means the reliability of prior knowledge for future events we can obtain by analyzing past events is on the decline. Therefore, we believe the forward-looking usage of Earth's surface observation images are crucial for fast response to incoming natural hazards and expediting hazards mitigation afterwards, such as flood mitigation activities (Eghbal et al., 2023) and flood risk analysis (Alabbad & Demir, 2022; Yildirim & Demir, 2022).

To date, the problem of predicting Earth's surface observation images (e.g., SAR, Sentinel-2, and Landsat images) with physics-informed approaches have not been well studied due to the complexity of the physical processes. The emergence of data-driven models (Sit et al., 2021a), especially deep learning models, allows us to explore problems with hard-to-describe complex processes (Xiang et al., 2021) from a viewpoint of data, making many out-of-reach problems in the past tangible at present. The RS research field is not an exception. Recently, Li et al. (2023) introduced a new research question – predicting Earth's surface observation images with independent physical variables. In their study, the authors synthesized Sentinel-1 SAR images at the pixel level using geomorphic datasets, SAR images obtained one revisit cycle (12 days) prior to the target time, and precipitation and soil moisture measurements obtained within 7 days prior to the target time. Building on top of that work, Li & Demir (2024) introduced two deep-learning-based frameworks, SA, and SS, to blend localized inputs with information from neighboring areas of target regions for improved performance.

Data-driven models, especially deep learning models, rely on large amounts of high-quality data (Demir et al., 2022). So far, we have a nonnegligible number of public datasets designed

especially for ML&DL-aided semantic segmentation, classification, object detection, change detection, and super-resolution applications (Schmitt et al., 2023; Demiray et al., 2021). In each of those sub-fields, the number of public datasets published has been growing fast over recent years as more data is becoming available and the quality of data is improving (Sit et al., 2021b). For instance, for ML/DL-aided flood inundation mapping tasks that is within the category of semantic segmentation, researchers created datasets with multimodal RS image generated with multispectral, hyperspectral, radar, and UVA sensors (Melancon et al., 2022; Mukherjee et al., 2023; Rahnemoonfar et al., 2021) and very-high-resolution (VHR) RS images (Li et al., 2023; Zhang et al., 2023). Researchers have also put a lot of efforts on developing big datasets that have global coverage for flood inundation mapping (Mateo-Garcia et al., 2021; Wieland et al., 2023). Unfortunately, as of today, we barely saw any openly accessible datasets that support deep-learning-based experiments on prospective Earth's surface observation image synthesis.

In this study, we aim at proposing a comprehensive dataset designed for the novel research question of predicting Earth's surface observation images with relevant physical input, such as precipitation, soil moisture, and geomorphic information. The dataset's scope is defined by 34 Sentinel-1 SAR images captured during the spring and summer of 2019 in the Midwest United States when the catastrophic 2019 Central US Flooding Event occurred. Eleven independent variables, including the previous Earth surface observations, precipitation, soil moisture, land cover, HAND, and DEM are incorporated for Earth surface observation image synthesis. In addition to validating predictions against real Earth observations, we included slope and reference flood map datasets to enable investigation of the usefulness of those predictions in downstream tasks, such as flood inundation mapping. The proposed dataset is aimed at facilitating fast analyses and scientific benchmarking for the Earth's surface observation image synthesis research question. Thanks to the diversity of items inside the dataset, custom datasets can easily be generated to explore the abovementioned research question with various approaches and configurations. By combining our dataset with other public datasets, researchers can explore a broader range of downstream research topics and applications, such as land cover classification and image generation, with far less effort on data collection and preparation.

2. Dataset and Methodology
2.1. Spatial and Temporal Coverage

The dataset contains 34 SAR images captured during the 2019 Central US flooding on different dates and in different regions from March 16 to June 23, 2019. Each of those SAR images covers about 75,000 km^2. The 2019 Central US flooding consisted of several consecutive events that happened in the Mississippi and Missouri River regions. The flood series were believed to be triggered by fast snow melt in the spring and several prolonged rainstorms followed in late spring and summer (Flanagan et al., 2020). The dataset covers regions that were severely affected by the 2019 Central US flood event in 11 states that are located on or adjacent to the Mississippi and Missouri River tributaries. Figure 1 depicts the extent of the dataset's coverage.
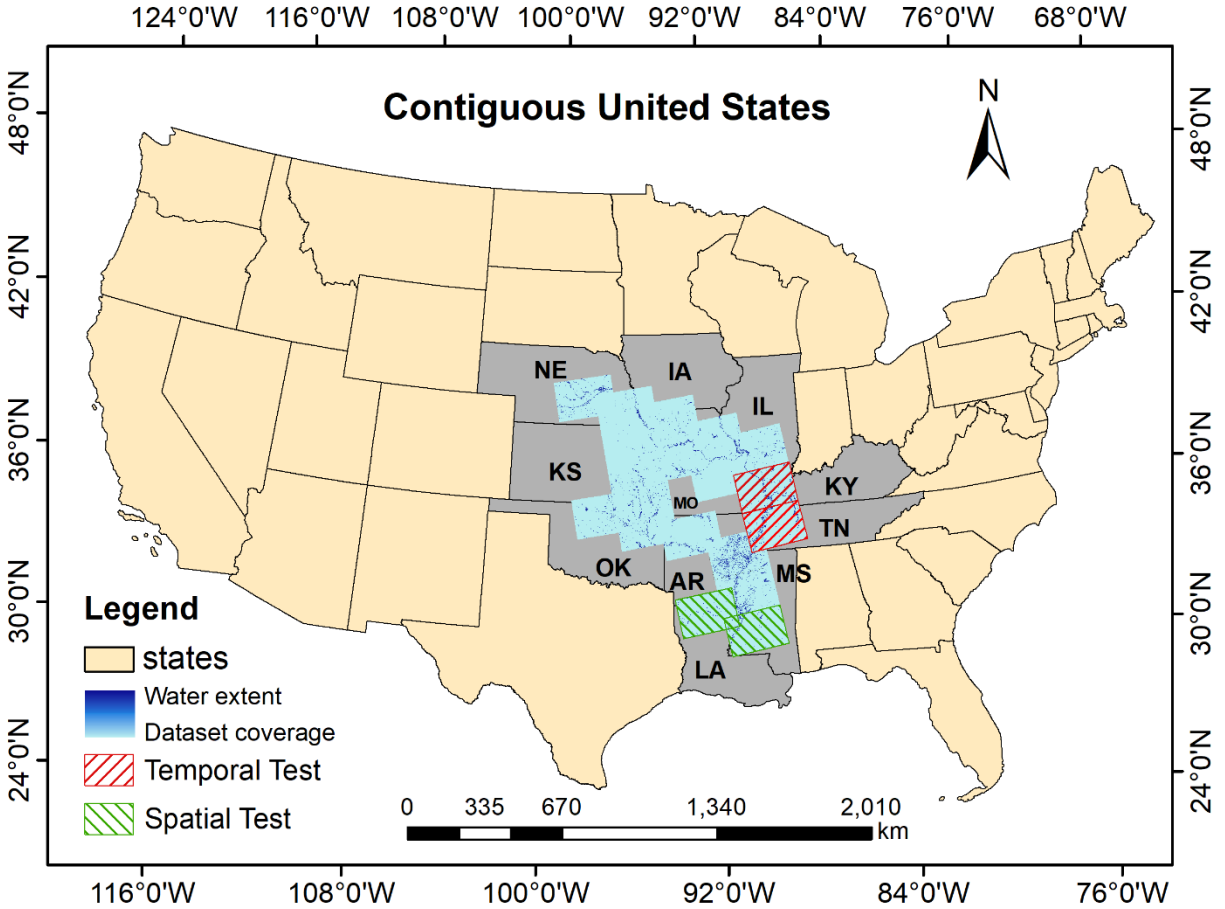
Figure 1. The extent of the dataset's coverage and its division. Note that some images overlap with others. This figure is adapted from Fig.1 of the work down by Li et al. (2023).

2.2. Composition of the Dataset

We collected several geomorphic and meteorological input items within the coverage of each of those 34 SAR images. Table 1 lists the data items incorporated in the dataset.

Table 1. Data items integrated in the dataset and the potential use cases.

Item	Spatial Resolution	Source	Potential Use Cases
SAR	10 m	GEE	Flood inundation mapping; wetland mapping; land cover classification; image translation; object detection
HAND	10 m	NFIE Data Repository	Flood inundation mapping; postprocessing
Landcover	10 m	ESA WorldCover V100	Change detection & analysis; environmental semantic segmentation

GPM v6 Precipitation (precipitationCal layer)	0.1 degree	GEE	Inter-comparison analysis; hydrological modeling; down-/up-scaling
SMAP Soil Moisture (ssm layer)	10,000 m	GEE	Inter-comparison analysis; drought monitoring; hydrological modeling; down-/up-scaling
DEM (USGS 3DEP)	10 m	GEE	Super resolution; environmental semantic segmentation; postprocessing
Slope (derived from ALOS DSM)	30 m	GEE	Environmental semantic segmentation; postprocessing
Reference Flood Map	10 m	High-Resolution Flood Inundation Archive	Result evaluation and validation

2.2.1. SAR Image Layers

The SAR images incorporated in the dataset are Sentinel-1 C-band SAR ground range detected products. Each SAR image in this study contains three bands – VH (vertical transmit/horizontal receive), VV (vertical transmit/vertical receive), and angle. Due to the similarity and correlation between VV and VH bands (Buono et al., 2023; Nguyen et al., 2021), we believe that it is unnecessary to include both bands in the dataset. We decided to include the VV band of each SAR image, as many previous studies, especially for water extent delineation, reported higher accuracy using this band over the results obtained from using the VH band (Markert et al., 2020; Tiwari et al., 2020; Twele et al., 2016). For simplicity, the VV band of each SAR image will be referred to as "SAR" or "SAR image" hereafter. As GEE has already had all SAR images gone through a comprehensive preprocessing workflow including orbit metadata update, thermal noise removal, and terrain correction (Moothedan et al., 2020), we applied a 7×7 Refined Lee filter to depress speckle noise. There are two SAR layers in the datasets. For each of the 34 SAR images mentioned previously, we will have a separate SAR that was captured at the exact same location but one revisit cycle (12 days) prior to the current one. Since those previous SAR layers share the spatial extent with the target SAR layers in pairs and were stacked together, we will continue to use "34 SAR images" instead of "68 SAR images".

2.2.2. Geomorphic Layers

Height Above Nearest Drainage (HAND) are normalized surface elevation values that represent the elevation differences between any hillslope (non-drainage) pixels and the nearest drainage pixels (pixels constantly underwater, such as river channel pixels) those hillslope pixels drain to (Nobre et al., 2011; Rennó et al., 2008). HAND has been widely used as an independent simplified flood model in flood inundation applications (Li & Demir, 2022; Li et al., 2023). In the realm of remote-sensing-aided flood mapping applications, HAND has been widely used as an auxiliary dataset in postprocessing (Li & Demir, 2023a; Zeng et al., 2020) and a key input layer for deep-learning-based surface flood mapping frameworks (Li & Demir, 2023b). Liu et al. (2016) created the 10-m resolution HAND dataset for the conterminous US (CONUS). The layer is

stored separately for 331 HUC6 units and is open for free download from NEFI Continental Flood Inundation Mapping Data Repository.

The land cover is the 10-m WorldCover 2020 v100 product. The data is freely accessible on GEE and EAS's website. WorldCover v100 product was created using Sentinel-1 SAR and Sentinel-2 images. It contains 11 classifications and has global coverage. We selected the WorldCover 2020 product because the WorldCover project was launched in 2019 and the ESA did not release the land cover map in the same year. The DEM layer is the USGS 3DEP 10-m seamless product that is openly available on GEE. The slope layer is derived from the Global 30 m ALOS DSM v3.2 product and was resampled to 10 m when exported from GEE. We first clipped those four geomorphic layers with the extent of each SAR image and then conducted a pixel-level alignment to make sure the pixels corresponding to the same ground location were well aligned along the channel (band) dimension.

2.2.3. Meteorological Layers

Our dataset incorporates five precipitation layers (precipitationCal layer) from the GPM v6 product. They are the cumulative precipitation over 24h, 48h, 72h, 120h, and 168h (up to 7 days) prior to the time each SAR image was captured. As the original spatial resolution of those precipitation layers is 0.1 degree (about 11,100 meters), we conducted ordinary kriging interpolation to make their resolution match with SAR images. Then, we conducted clip and pixel-level alignments.

2.2.4. Surface Condition Layers

Our dataset contains two soil moisture layers, with both being the ssm layers from the NASA-USDA SMAP soil moisture data available on GEE. As the data in the SMAP dataset on GEE are updated every three days, we selected the two measurements that were temporally closest and within 7 days prior to the capture time of any SAR images in our dataset. Like the precipitation layers, the soil moisture layers also come with a coarse resolution. The same pre-processing from the previous subsection, geo-interpolation – clip – pixel-level alignment, was applied to the two soil moisture layers.

2.2.5. Reference Flood Map Layers

The reference flood maps in the dataset come from the high-resolution flood inundation archive (2016-the present) introduced by Yang et al. (2021). The archive contains 10-m flood maps for CONUS generated with ESA Sentinel-1 SAR images using the automated Radar Produced Inundation Diary (RAPID) system. The authors compared this flood map dataset with the USGS Dynamic Surface Water Extent (DSWE) product and reported a substantial agreement and satisfying accuracy (Yang et al., 2021). The dataset is openly available on the Amazon Web Service (AWS) platform.

2.2.6. Dataset Summary

We unified the scope and the resolution of all those data items discussed above with the corresponding SAR images so that pixels of different data layers are well aligned for the same location. With the alignment done, layers were then stacked on top of each other. Finally, those image layers were sliced into 395,363 image patches with the dimension of each layer being 256-by-256 pixels. It is worth noting that not all items listed in Table 1 are stacked and stored together. As our dataset is multipurpose, we need to balance between simplicity (putting everything together) versus flexibility (easy referencing for different applications). Specifically, the slope, DEM, and reference flood map patches were stored separately, whereas the patches of all the other data layers were stacked and stored together.

The image patches from the original SAR images with ID 52FC and 8814 were saved as a temporal robustness test set (the area covered by the red slash in Figure 1). Similarly, the patches from the SAR images with ID 1544 and 086E are saved for a spatial robustness test set (area covered by the green slash in Figure 1). Those robustness test patches can be used to test the generalization capability of the models. In cases where the generalization test is not necessary, they can also be used along with other images in the train-validation-test split. The spatial robustness images have limited overlapped or no overlapped area with other images and the temporal robustness test images are randomly selected among the remaining images with the spatial robustness test images excluded.

3. Benchmark Tasks and Evaluation Metrics

3.1. Overview of Benchmark Tasks

We will introduce three sample tasks to demonstrate the usefulness of our dataset as well as to provide benchmark performance for future studies for comparison. The tasks include Earth's surface observation prediction with localized input variables; Earth's surface observation prediction through blending localized and neighboring input variables; and downstream application of the Earth's surface predictions. In this study, we adopted flood inundation mapping as a downstream application to evaluate the usefulness of the synthesized Earth's surface images from a different point of view. In addition to those three sample tasks, the dataset can also be used in super resolution, land cover classification, and image translation tasks. Moreover, the sample tasks can also be further explored with different configurations, such as changing the way the information in neighboring areas will be integrated and changing the number of neighbors being considered.

The task of predicting Earth's surface observation images can be interpreted as building a regression model using the geomorphic, meteorological, and surface condition information to predict (or simulate) the backscatter values of SAR images at the pixel level. For the localized prediction, all input data items come from the target region we are predicting SAR backscatters for. Whereas for the other scenario, the connection between the target region and its surroundings is considered. Specifically, we will consider the impact of neighboring regions on the target by adding some variables obtained in the neighboring regions into our prediction framework when

generating the backscatters for the target location. Once we have the SAR backscatter predictions, we can evaluate them against the real SAR backscatter values at those target locations. In addition, we can evaluate their usefulness by validating the downstream products against some separate reference. In this study, the downstream product is the flood inundation map that will be generated using the SAR predictions. Figure 2 illustrates the conceptual design of the three tasks mentioned above.
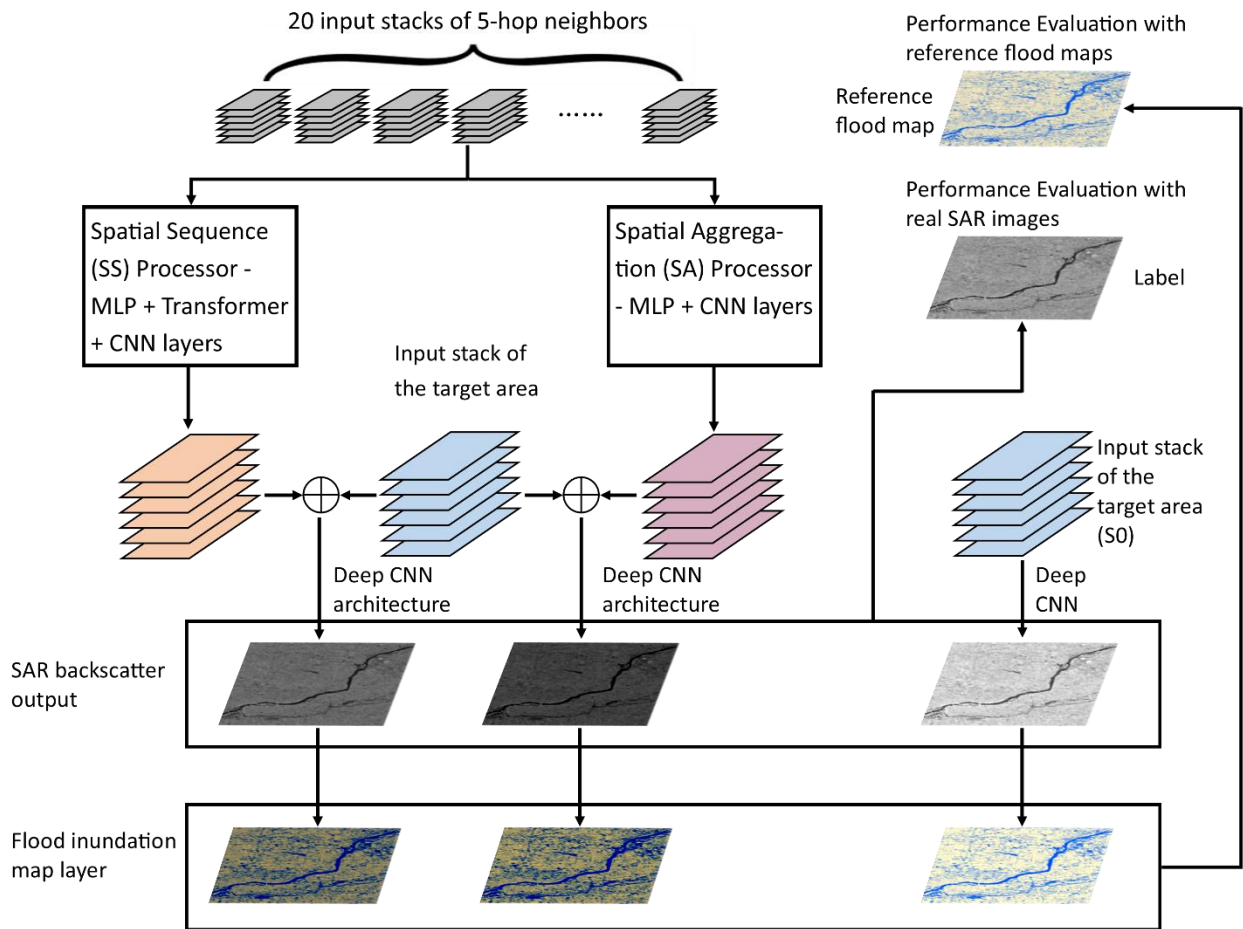

Figure 2. The conceptual design of the three sample tasks utilizing the dataset. Predicting SAR images with the localized data only (S0); predicting SAR images by blending the localized data with neighboring input with the Spatial Sequence approach (SS); predicting SAR images by blending the localized data with neighboring input with the Spatial Aggregation approach (SA).

Information considered in neighboring areas are five precipitation and two soil moisture layers, as the precipitation and soil moisture have direct impacts on adjacent areas through surface and soil water flow. Pixels with the same row and column indexes in an input image for the target and neighboring location do not refer to the same location, as the spatial extent of the two images are not the same. For instance, the pixel in row #32, column #89 in a neighboring input patch can be dozens of kilometers away from the pixel with the same row and column

numbers in the target input patch. Therefore, we cannot do a band-wise addition or simply stack neighboring input patches onto the localized input patches. To solve that issue, we used the Spatial Sequence (SS) approach and Spatial Aggregation (SA) approaches to approximate the overall impact on the target area from its neighbors. As discussed above, due to the intrinsic spatial requirements of image processing, SA and SS can only simulate a coarse area-to-area effect rather than a precise pixel-to-pixel relationship.

The idea of SA is to aggregate the information from neighboring areas through a Multi-Layer Perceptron (MLP) layer, whereas SS derive the aggregated information by handling the information from neighbors at different distance to the target as a spatial sequence. Then, the aggregated information from neighboring areas will be fed into several CNN layers to resume the original image dimension so that the resulting layers with the same dimensions as the localized images can be added or stacked with the localized image patches. As the objective of this work is to introduce the dataset that supports the above-mentioned complex experiments, rather than introducing the algorithms themselves, we highly recommend readers check the previous work by Li & Demir (2024) where we introduced how information from the target and its neighbors are blended and how the SS and SA are implemented in detail.

In this work, we accepted the configurations for information blending introduced in the work done by Li & Demir (2024). Specifically, we will consider neighbors within 5 hops (5 moves in total, following D8 flow directions) of the target image patch. The seven-band (five precipitation plus two soil moisture) input stack from any neighboring image patches will first be reduced to a vector with a length of seven by taking the average among each 2D plane. Then, the vectors from neighbors at the same distance to the target will be averaged again. As a result, the neighboring information for any target will be a 20×7 matrix, where 20 represents all possible distances, a neighbor can be at from the target within the 5-hop scope and 7 represents the 5 aggregated precipitation plus 2 aggregated soil moisture values derived from all neighbors at a specific distance. Figure A1 and Table A1 in the Appendix section present the definition of neighbors within the 5-hop scope of any target and the 20 possible different distances to any target image patches.

3.2. Evaluation Matrixes

The evaluation of the three sample tasks discussed in the previous subsection includes evaluating the predicted SAR images and flood maps derived from the predicted SAR images. Therefore, we utilized two sets of metrics to evaluate those results separately. Mean Absolute Error (MAE), Nash-Sutcliffe Efficiency (NSE), Sinkhorn Divergences (DS), and an assembled accuracy index (AAI) is used to evaluate the accuracy of predicted SAR images. Intersection over Union (IoU), F1 Score (F1), and Accuracy (A) is used to evaluate the accuracy of the flood maps derived from the predicted SAR images. Those indexes calculate as follow:

$$MAE = \frac{\sum_{i=1}^{n}|pred_i - target_i|}{n}$$

where *pred* and *target* is the predicted and target (real) SAR image, respectively, and n represents the total number of pixels in the predicted or the target image. MAE is a non-negative value with 0 being the best possible value.

$$NSE = 1 - \frac{\sum_{i=1}^{n}(pred_i - target_i)^2}{\sum_{i=1}^{n}(target_i - \overline{target})^2}$$

where $\overline{target}$ is the averaged backscatter value of all target backscatters. NSE ranges from -infinity to 1, with 1 being the best possible value and a negative value means the prediction is worse than simply taking the mean value of all observations.

$$SD(pred, target) = OT - \frac{1}{2}OT(pred, pred) - \frac{1}{2}OT(target, target)$$

SD measures the geometric divergence in terms of the dissimilarity between the probability distribution of the prediction and the target. OT is the Optimal Transport problem with entropic regularization defined by Oneto et al. (2020). Similar to MAE, SD has a non-negative value. The smaller SD is, the more accurate the predictions are.

$$AAI = \frac{1}{1 + MAE} + \frac{1}{1 + SD} + NSE$$

AAI was introduced in a previous work done by Li et al. (2023) to give a comprehensive description of the accuracy of the model taking into account MAE, SD, and NSE. AAI is created in a way that the larger each component is, the higher AAI is and the more accurate the predictions are.

$$IoU = \frac{TP}{TP + FP + FN}$$

TP represents correct positive (flooded) pixels marked by the model, FP are incorrect flooded pixels marked by the model, and FN are incorrect negative (dry) pixels from the model prediction. IoU ranges in [0, 1] with 1 meaning the predictions overlap perfectly with the reference.

$$F1 = \frac{TP}{TP + \frac{1}{2}(FP + FN)}$$

F1 combines the precision and recall scores of a model and thus can measure the accuracy and the completeness of the predicted flooded pixels at the same time. Similar to IoU, F1 also ranges from 0 to 1, with 1 being the best possible value.

$$A = \frac{TP + TN}{TP + FP + FN + TN}$$

A measures the ratio of correct predictions over all predictions. *A* ranges from 0 to 1, with 1 being the best possible value. Depending on the type of result to be evaluated (SAR images or flood maps), we calculated corresponding indexes and stored them separately with the same index values from other predicted patches. We then analyzed the statistical characteristics with the computed index values within each respective index list.

3.3. Details of Model and Task Implementation

All deep learning frameworks in this study, including those for SAR image prediction and for the downstream semantic segmentation (surface water inundation mapping), were implemented using PyTorch., We utilized four NVIDIA Tesla K80 GPUs for the two SAR prediction tasks and two Tesla K80 GPUs for the downstream semantic segmentation. For fast comparison and analyses, we integrated several off-the-shelf implementations of CNN architectures from Segmentation Models into our models for SAR backscatter prediction and the downstream flood inundation extent delineation tasks. Segmentation Models is an open-access project that allows easy creation of 9 state-of-the-art CNN models with 500+ pre-trained encoders. Segmentation Models (2024) can be accessed through GitHub repository.

For the localized SAR prediction (will be referred to as Task 1 hereinafter), the performance of four widely used CNN models, namely, Unet, PSPnet, MAnet, and DeepLabV3++, will be compared to the persistence benchmark that simply takes the previous SAR image as the prediction. All models will be trained, validated, and tested on a cluster of images of size 11601 256×256 image patches split following a ratio of 7 (train): 2 (validate): 1 (test). This cluster of image patches is obtained by filtering all patches within the 30 SAR images' scope with a ratio of permanent water pixels (land cover class 80 or 90 in the land cover layer) being no less than 10%. This filtering step is task-specific and is changeable (e.g., change filtering criteria or threshold) and optional according to different applications. For our sample tasks, we do not want to focus on image patches with to too few water bodies, as surface conditions of areas away from permanent water bodies, such as hillslope regions, are quite consistent during flooding events as they are barely affected by inundation. Therefore, predicting the surface conditions for those areas over a short duration of time is unnecessary. In addition to the inter-model comparison, we also tested the generalizability of one model on one of the four saved robustness test sets.

For the task of predicting SAR images with both localized and neighboring information (will be referred to as Task 2 hereinafter), we generated a different custom dataset from the previous one. As we want to compare the performance from S0 (the same as Task 1), SA, and SS, we need to make sure they work on the same dataset in which each target image should have neighbors, so that SA and SS are applicable. Therefore, we removed images with no neighbors from the previous custom dataset. In addition, as the generalizability of the model was validated in the previous task and we would not conduct robustness test again in this task again, we included qualified images from those four robustness test sets. The custom dataset for this task contains

8,932 images with 256 × 256 pixels and was also split into the train-validation-test sets following a 7:2:1 ratio. Since the custom dataset for this task is different from the previous custom dataset, the persistence benchmark performance for the new dataset needs to be computed separately.

For the task of evaluating flood maps derived from the predicted SAR image (will be referred to as Task 3 hereinafter), all previous SAR predictions can be used. To avoid redundant comparison, we will adopt the SAR predictions from one model in Task 1, generate flood maps with Otsu thresholding (a non-deep-learning binary classification method) and Unet (a deep learning structure that is well known for semantic segmentation tasks) from those synthesized images and real SAR images, and compare the resulting flood maps with reference flood maps.

4. Results and Discussion

4.1. Task 1 - Localized SAR Prediction

We trained four different CNN architectures, namely, MAnet, Unet, PSPnet, and DeepLabV3++, with the same encoder – Resnet 50. All models were trained, validated, and tested using the same custom dataset described in subsection 3.3. All hyperparameters, such as the number of epochs, learning rate, batch size, and optimizer were kept the same. Table 1 lists the performance of each model on the test set, as well as the benchmark performance of persistence. As shown in Table 2, all four deep learning models significantly outperformed the persistence benchmark. Among the four deep learning models, the performance of MAnet and Unet are comparable and rank at the top, followed by DeepLabV3++. PSPnet generated the worst performance.

Table 2. Performance of four different deep learning architectures compared to the persistence benchmark.

Item	MAE (mean)	MAE (median)	SD (mean)	SD (median)	NSE (mean)	NSE (median)	AAI (mean)	AAI (median)
Persistence Benchmark	2.20	1.93	1164.58	833.26	0.58	0.73	0.91	1.07
MAnet	1.55	1.40	602.23	424.38	0.80	0.85	1.20	1.26
Unet	1.54	1.40	597.78	423.63	0.80	0.85	1.20	1.26
PSPnet	1.69	1.57	672.76	522.2	0.77	0.81	1.16	1.20
DeepLabV3++	1.60	1.44	633.33	437.04	0.79	0.83	1.19	1.25

Since all four models have the same encoder, we know that it is the model architecture that led to performance discrepancies. Due to the fast evolution of deep learning architectures, it is impossible to give an exhaustive comparison including all possible combinations of the existing architectures and encoders here and it is also not the objective of this study. For researchers who want to validate the efficacy of a new model, they may consider following our approach of comparison – keeping the encoder and all hyperparameters the same, so that performance differences can be attributed to the new model architecture.

Figure 3 depicts the AAI and NSE of predictions generated with the five approaches listed in Table 2 using all samples in the test set. The two sub-plots indicate that although the mean and median values of the evaluation indexes of MAnet and Unet are quite similar, MAnet did a slightly better job than Unet as samples of the former were more concentrated towards higher values of AAI and NSE.
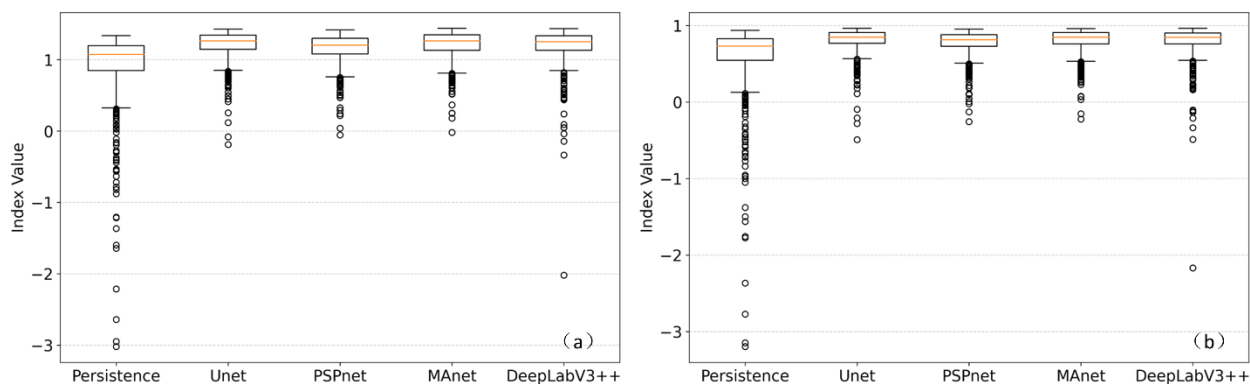

Figure 3. Boxplot of AAI (a) and NSE (b) with predictions generated with the persistence assumption and using the four deep learning models on the test set.

Figure 4 depicts SAR predictions using MAnet along with real (target) SAR images in 12 different scenes. Six of those scenes come from the test set and the others are from one spatial robustness test set (086E) that the model had never seen during training, validation, and testing stages. Fine-tuning was not conducted on the spatial robustness test set. Figure 4 clearly shows that deep learning models can predict Earth's surface observation image (SAR, in this study) with enough details, even in regions with complex river channel geometry, such as Scenes #4 and #6 of the test set and #2 and #5 of the robustness test set. The robustness and generalizability of the model on "out-of-scope" data is also satisfying.

4.2. Task 2 - SAR Images with Localized and Neighboring Information

In Task 2, MAnet was adopted as the model S0 and it was trained only with localized data – data that has the same scope as the target SAR image, just as what we did in Task 1. In contrast, SA and SS were trained with not only the localized data but also the aggregated input information from surrounding areas of each target image. Table 3 lists the performance from each approach. For SA and SS, in addition to those indexes obtained by comparing against target SAR images, we also listed the performance improvement compared to S0 in percentage. As we mentioned in subsection 3.3, we generated a different custom dataset for Task 2, and this is the reason the persistence benchmark performance in Table 3 and Table 2 are different.

Table 3 shows that considering neighboring information can further improve model performance. Compared to S0, two error terms (MAE and SD) of SA and SS were lower while the two accuracy indexes (NSE and AAI) were higher. In addition to that, Table 3 shows that the way the neighboring inputs are considered also has an impact. In general, SS was doing better

improving the mean value of the four evaluation indexes whereas SA did a better job for the medians.
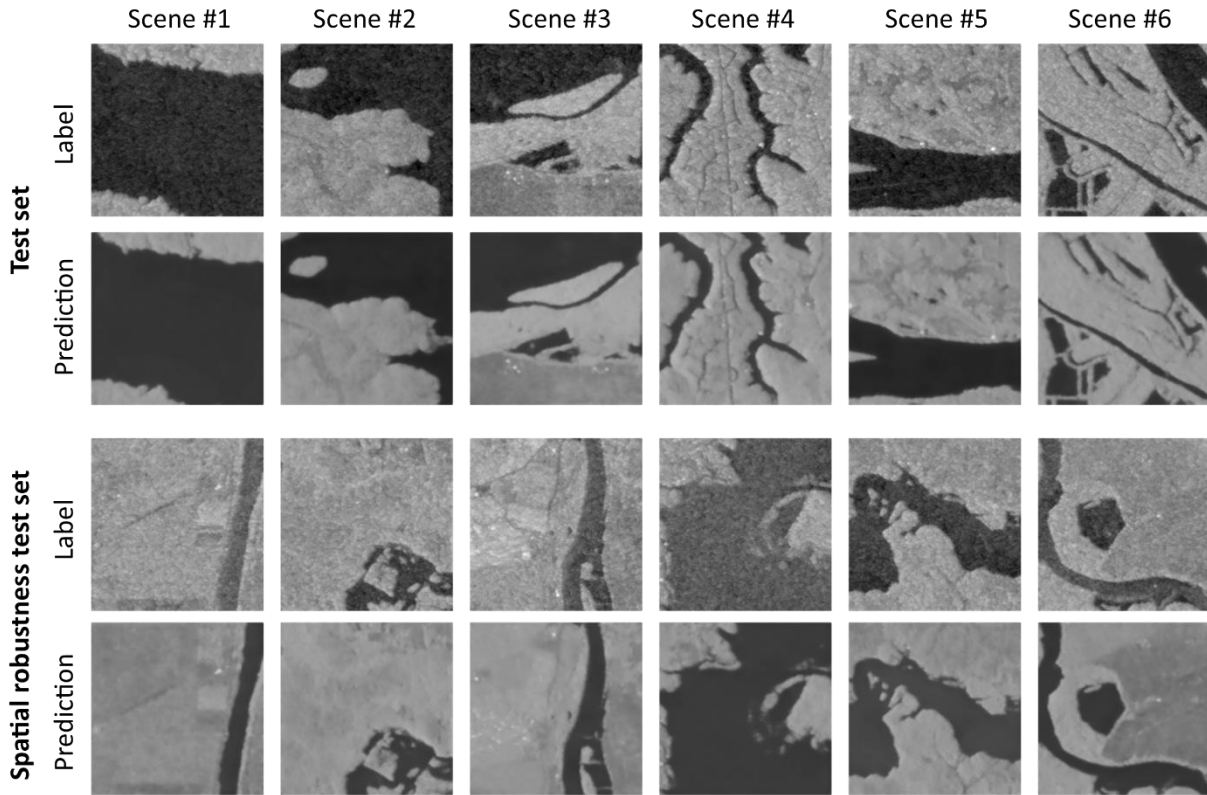

Figure 4. Visualization of the predicted SAR with MAnet versus the target (real) SAR in six scenes from the test set and six scenes from the spatial robustness test set, respectively.

Table 3. Performance of different model configurations that blend/not blend local and neighboring input.

	Item	MAE (mean)	MAE (median)	SD (mean)	SD (median)	NSE (mean)	NSE (median)	AAI (mean)	AAI (median)
	Persistence Benchmark	2.21	1.97	1151.37	838.99	0.59	0.74	0.92	1.08
	S0	1.60	1.43	637.47	452.65	0.78	0.86	1.18	1.27
SA	Statistics	1.57	1.40	611.65	430.91	0.79	0.87	1.19	1.28
	Improvement against S0 (%)	-1.88	-2.10	-4.05	-4.80	1.28	1.16	0.85	0.79
SS	Statistics	1.56	1.41	594.88	439.28	0.79	0.86	1.20	1.28
	Improvement against S0 (%)	-2.50	-1.40	-6.68	-2.95	1.28	0.00	1.69	0.79

Figure 5 shows boxplots of AAI and NSE of the four approaches listed in Table 3. As shown in Figure 5, predictions from S0, SA, and SS are noticeably better than those from the persistence benchmark. In contrast, the difference among S0, SA, and SS are not so obvious visually, and lies more in the distribution of "outliers" (samples for which models failed to generate as good results, not real outliers). Figure 6 shows the predicted SAR image using the S0, SA, and SS versus the real SAR image (Label) in six scenes from the test set. We can see that the visual difference between the three models is hardly noticeable.
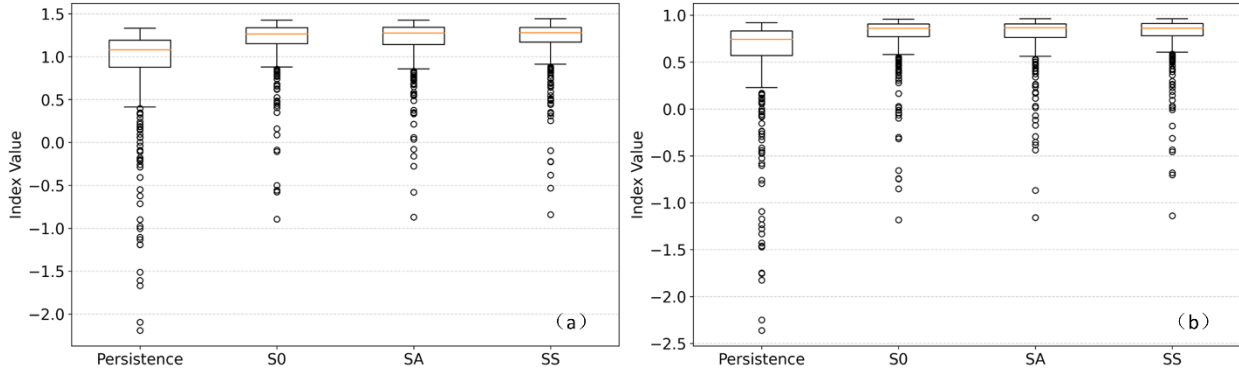

Figure 5. Boxplot of AAI (a) and NES (b) of the persistence benchmark, S0, SA, and SS on the test set.

4.3. Task 3 - Flood Maps from Predicted SAR Images

Task 3 demonstrates how the dataset proposed in this study can be used in downstream tasks, such as flood inundation mapping. In this study, we adopted a DL approach – Unet, a widely used semantic segmentation (pixel-level classification) model introduced by Ronneberger et al. (2015) and a non-DL approach – Otsu thresholding that conducts pixel-level binary classification automatically by analyzing the histogram of all pixels (Nobuyuki Otsu, 1979). The Unet segmentation model was trained with HAND, slope, and the real or predicted SAR image that are all included in the dataset proposed in the study. SAR image predictions from all frameworks tested previously (results from four DL models in Task 1 plus those from S0, SS, and SA in Task 2) can be used to generate flood maps. To avoid redundant comparisons and results, we used the predictions derived from the MAnet in Task 1.

Table 4 lists the accuracy of flood maps generated from real (target) and predicted SAR images using both the DL and non-DL methods compared to the reference maps. Compared to flood maps derived from the real SAR images, results from the synthesized SAR showed a slightly worse consistency with the reference map. However, in general, the indexes of the flood maps from SAR predictions are still satisfying. We saw that for flood maps derived from the fake SAR images, those obtained with Otsu were slightly better than those obtained using the Unet. This indicates that error and uncertainty will accumulate along the entire procedure. Given input with uncertainties and errors, deterministic methods, such as the Otsu thresholding, can be more

robust, as the methods themselves will not introduce new uncertainties, and therefore may lead to better results.
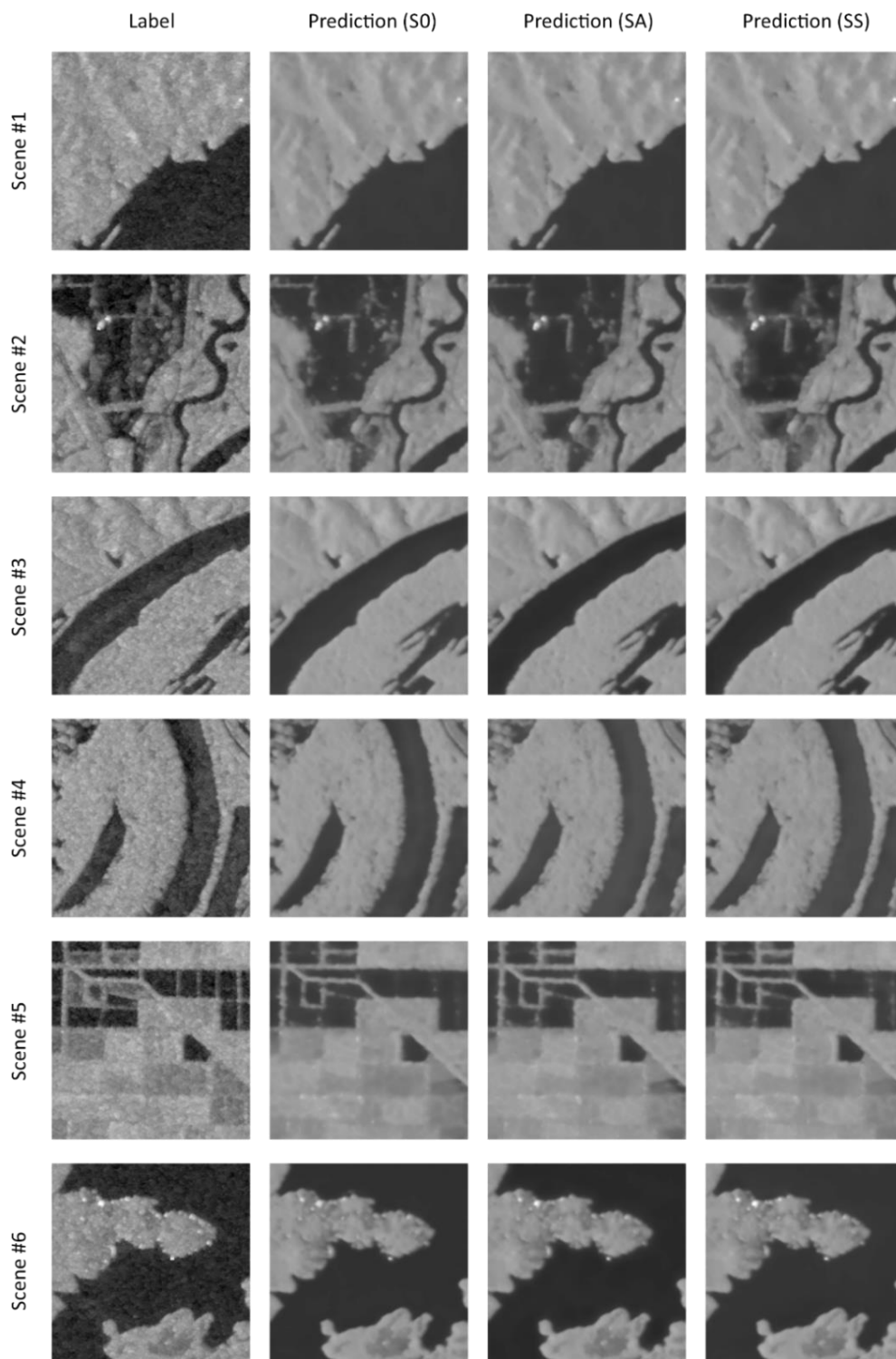

Figure 6. SAR image prediction with S0, SA, and SS versus the real SAR images in six scenes from the test set.
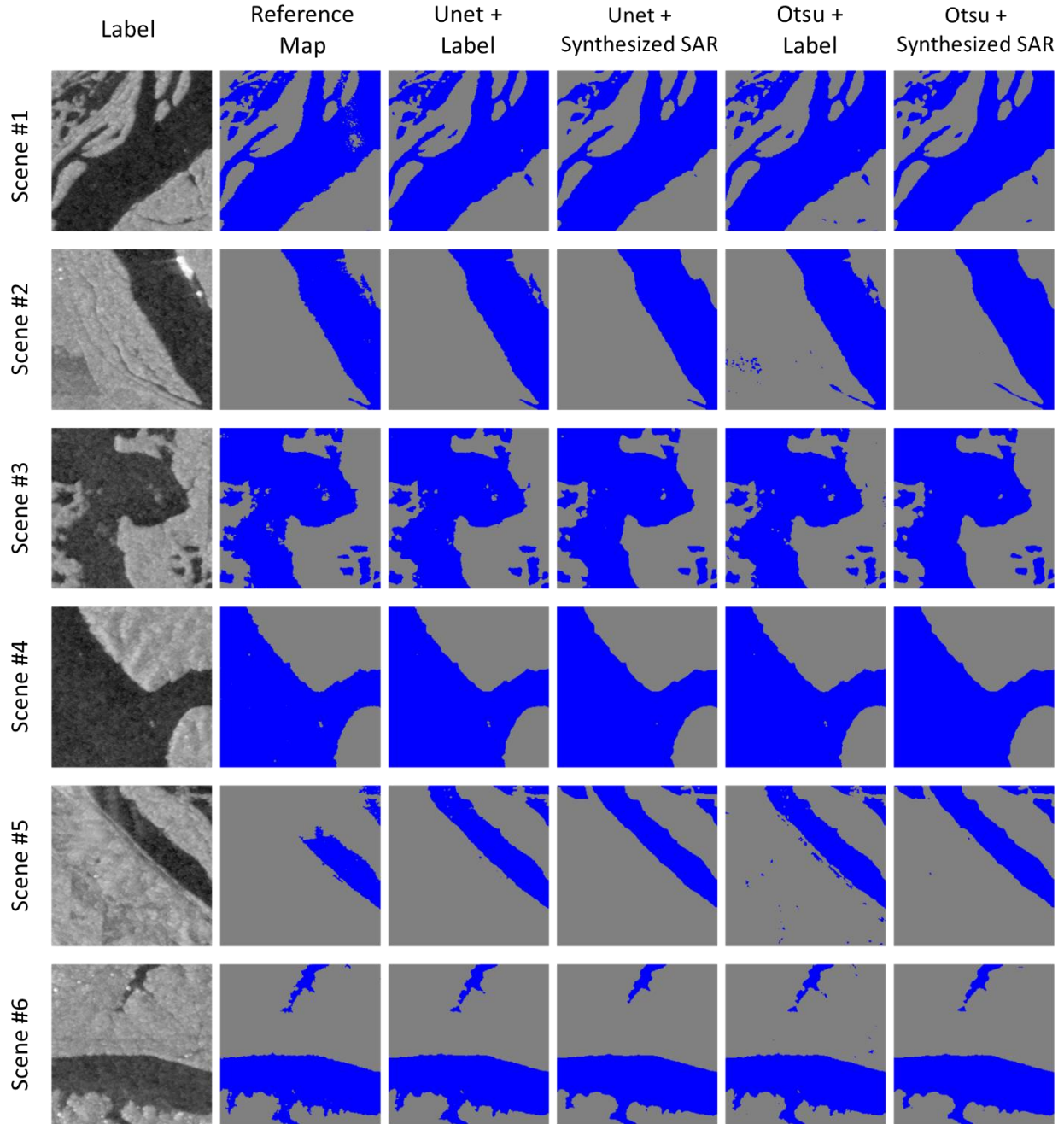
Figure 7. Flood inundation maps derived from the synthesized SAR image patches with Otsu and Unet compared with those derived from the real SAR images and the reference flood map.

Figure 7 shows six examples of target SAR images, reference flood maps, and the four resulting flood maps with real and synthesized SAR images. We noticed that results from Otsu thresholding can be a bit noisier (scattered dry pixels in flooded regions and scattered flooded pixels in dry regions) in some local regions, such as Scenes #1, #2, #5, and #6. Comparatively, Otsu with label (real) SAR is noisier than Otsu with the synthesized SAR. This is mainly because of the information loss during the convolution process of CNN architectures (Guo et al., 2022),

The loss of details has a de-noising effect on the pixel-level predictions. On the other hand, it can suppress misclassifications due to noise, especially for segmentation tasks (Li & Demir, 2023b). The quantitative and visual evaluation showed clearly that structural features on flood maps derived from synthesized SAR images were consistent with those on reference flood maps and proved the usefulness of synthesized Earth's surface observation images in downstream applications.

Table 4. Evaluation of usefulness of the predicted SAR images in flood extent mapping with both DL and non-DL methods against results from real SAR images

	IoU (mean)	IoU (median)	F1-Score (mean)	F1-Score (median)	Accuracy (mean)	Accuracy (median)
Real SAR (DL)	0.90	0.95	0.94	0.97	0.97	0.99
Synthesized SAR (DL)	0.82	0.90	0.89	0.95	0.94	0.98
Real SAR (Otsu)	0.86	0.92	0.91	0.96	0.95	0.98
Synthesized SAR (Otsu)	0.83	0.90	0.90	0.95	0.94	0.97

5. Conclusion

In this study, we proposed a comprehensive dataset for Earth surface observation image synthesis tasks. The dataset contains Sentinel-1 SAR imagery, precipitation, soil moisture, land cover, HAND, slope, DEM, and reference flood maps to allow a thorough performance evaluation on not only the synthesized Earth surface observation images, but also in downstream tasks. We defined three sample tasks to demonstrate the usefulness of the dataset: Task 1 – synthesizing Earth surface images with localized input; Task 2 – synthesizing Earth surface images with both localized input and precipitation and soil moisture information obtained from neighboring areas; Task 3 – investigating the usefulness of synthesized images in flood inundation mapping through semantic segmentation with a deep learning model and with a deterministic automatic thresholding method.

Although the dataset has a specific spatial and temporal focus on the catastrophic 2019 Central US flood events that occurred on or near the Mississippi and Missouri River tributaries during the spring and summer of 2019, we believe that any future models and architectures that can bring record-breaking performance with this dataset will provide transplantable insights into Earth observation image synthesis problems for other regions around the world. We maintained a carefully determined balance between simplicity and flexibility when processing and organizing items in the dataset, to ensure easy access to different sub-components of each sample for various application purposes and to allow easy generation of custom datasets for different tasks.

This dataset can be an essential building block that contributes to the forward-looking usage of Earth surface observation images.

6. Dataset and Code Availability

Benchmark dataset and sample model codes are openly available at the GitHub repository: https://github.com/uihilab/EarthObsNet

7. Appendix

Figure A1 shows an example of a target and all its neighbors within 5-hop distance. Each grid represents an image patch. The median DEM value of each patch is used to determine the D8 flow direction.
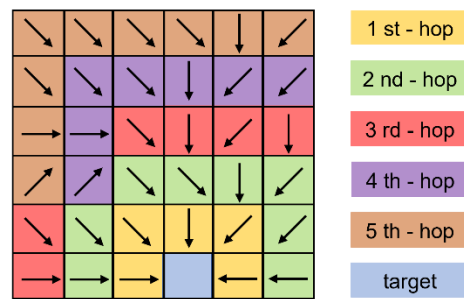

Figure A1. An example of 5-hop neighbors of a target image patch. The figure was adapted from Figure 3 of the work done by Li & Demir (2024).

Table A1 lists all possible distances of an adjacent patch from the target. As we are using D8 flow direction, the distance can be represented by different combinations of diagonal and non-diagonal moves from any neighboring patch to the target.

Table A1. All possible distance combinations within the 5-hop scope of any target patches. The table was adapted from Table 1 of the work done by Li & Demir (2024).

Hop	Possible Distance Combinations ($\times$ No. of pixels on the side $\times$ pixel length)					
1st	1	$\sqrt{2}$	-	-	-	-
2nd	2	$1+\sqrt{2}$	$2\times\sqrt{2}$	-	-	-
3rd	3	$2+\sqrt{2}$	$1+2\times\sqrt{2}$	$3\times\sqrt{2}$	-	-
4th	4	$3+\sqrt{2}$	$2+2\times\sqrt{2}$	$1+3\times\sqrt{2}$	$4\times\sqrt{2}$	-
5th	5	$4+\sqrt{2}$	$3+2\times\sqrt{2}$	$2+3\times\sqrt{2}$	$1+4\times\sqrt{2}$	$5\times\sqrt{2}$

8. References

Alabbad, Y., & Demir, I. (2022). Comprehensive flood vulnerability analysis in urban communities: Iowa case study. *International Journal of Disaster Risk Reduction*, *74*, 102955. https://doi.org/10.1016/J.IJDRR.2022.102955

Ali, A. U., & Ogie, R. (2017). Social media and disasters: Highlighting some wicked problems. *IEEE Technology and Society Magazine*, *36*(4). https://doi.org/10.1109/MTS.2017.2763450

Buono, A., Inserra, G., Abbasi, F. R., & Migliaccio, M. (2023). Multi-Frequency and Multi-Polarisation Analysis of the Scattering From Offshore Wind Turbines. *IGARSS 2023 - 2023 IEEE International Geoscience and Remote Sensing Symposium*, 1692–1695. https://doi.org/10.1109/IGARSS52108.2023.10281713

Cikmaz, B. A., Yildirim, E., & Demir, I. (2023). Flood susceptibility mapping using fuzzy analytical hierarchy process for cedar rapids, iowa. International journal of river basin management, (just-accepted), 1-24.

Demir, I., Xiang, Z., Demiray, B., & Sit, M. (2022). WaterBench-Iowa: a large-scale benchmark dataset for data-driven streamflow forecasting. Earth system science data, 14(12), 5605-5616.

Demiray, B. Z., Sit, M., & Demir, I. (2021). DEM super-resolution with efficientNetV2. arXiv preprint arXiv:2109.09661.

Eghbal Akhlaghi, V., Campbell, A. M., & Demir, I. (2023). The Flood Mitigation Problem in a Road Network. arXiv e-prints, arXiv-2302.

Fang, Z., Wang, Y., Peng, L., & Hong, H. (2021). Predicting flood susceptibility using LSTM neural networks. *Journal of Hydrology*, *594*, 125734. https://doi.org/10.1016/j.jhydrol.2020.125734

Flanagan, P. X., Mahmood, R., Umphlett, N. A., Haacker, E., Ray, C., Sorensen, W., Shulski, M., Stiles, C. J., Pearson, D., & Fajman, P. (2020). A Hydrometeorological Assessment of the Historic 2019 Flood of Nebraska, Iowa, and South Dakota. *Bulletin of the American Meteorological Society*, *101*(6), E817–E829. https://doi.org/10.1175/BAMS-D-19-0101.1

Guo, Z., Wu, L., Huang, Y., Guo, Z., Zhao, J., & Li, N. (2022). Water-Body Segmentation for SAR Images: Past, Current, and Future. In *Remote Sensing* (Vol. 14, Issue 7). https://doi.org/10.3390/rs14071752

Li, Y., Dang, B., Li, W., & Zhang, Y. (2023). *GLH-Water: A Large-Scale Dataset for Global Surface Water Detection in Large-Size Very-High-Resolution Satellite Imagery*. https://arxiv.org/abs/2303.09310v1

Li, Z., & Demir, I. (2022). A comprehensive web-based system for flood inundation map generation and comparative analysis based on height above nearest drainage. Science of The Total Environment, 828, 154420.

Li, Z., & Demir, I. (2023a). Flood Sequence Mapping with Multimodal Remote Sensing Under the Influence of Dense Vegetation: Mississippi River Case Study. *EarthArXiv*. https://doi.org/10.31223/X5909M

Li, Z., & Demir, I. (2023b). U-net-based semantic classification for flood extent extraction using SAR imagery and GEE platform: A case study for 2019 central US flooding. *Science of The Total Environment*, *869*, 161757. https://doi.org/10.1016/J.SCITOTENV.2023.161757

Li, Z., & Demir, I. (2024). Better localized predictions with Out-of-Scope information and Explainable AI: One-Shot SAR backscatter nowcast framework with data from neighboring region. *ISPRS Journal of Photogrammetry and Remote Sensing*, *207*, 92–103. https://doi.org/10.1016/J.ISPRSJPRS.2023.11.021

Li, Z., Duque, F. Q., Grout, T., Bates, B., & Demir, I. (2023). Comparative analysis of performance and mechanisms of flood inundation map generation using Height Above Nearest Drainage. *Environmental Modelling & Software*, *159*, 105565. https://doi.org/10.1016/J.ENVSOFT.2022.105565

Li, Z., Xiang, Z., Demiray, B. Z., Sit, M., & Demir, I. (2023). MA-SARNet: A one-shot nowcasting framework for SAR image prediction with physical driving forces. *ISPRS Journal of Photogrammetry and Remote Sensing*, *205*, 176–190. https://doi.org/10.1016/J.ISPRSJPRS.2023.10.002

Liu, Y. Y., Maidment, D. R., Tarboton, D. G., Zheng, X., Yildirim, A., Sazib, N. S., & Wang, S. (2016). A CyberGIS Approach to Generating High-resolution Height Above Nearest Drainage (HAND) Raster for National Flood Mapping. *The Third International Conference on CyberGIS and Geospatial Data Science*, *August*, 1–5. https://doi.org/10.13140/RG.2.2.24234.41925/1

Markert, K. N., Markert, A. M., Mayer, T., Nauman, C., Haag, A., Poortinga, A., Bhandari, B., Thwal, N. S., Kunlamai, T., Chishtie, F., Kwant, M., Phongsapan, K., Clinton, N., Towashiraporn, P., & Saah, D. (2020). Comparing Sentinel-1 surface water mapping algorithms and radiometric terrain correction processing in southeast Asia utilizing Google Earth Engine. *Remote Sensing*, *12*(15), 2469. https://doi.org/10.3390/RS12152469

Mateo-Garcia, G., Veitch-Michaelis, J., Smith, L., Oprea, S. V., Schumann, G., Gal, Y., Baydin, A. G., & Backes, D. (2021). Towards global flood mapping onboard low cost satellites with machine learning. *Scientific Reports 2021 11:1*, *11*(1), 1–12. https://doi.org/10.1038/s41598-021-86650-z

Melancon, A., Giezendanner, J., Zhang, Z., Mukherjee, R., Gurung, I., Tellman, B., & Molthan, A. (2022). *FloodPlanet: High-Resolution Commercial Imagery for Training and Validation of Deep Learning-Based Models of Inundation Extent*.

Moothedan, A. J., Dhote, P. R., Thakur, P. K., & Garg, V. (2020). Automatic Flood Mapping using Sentinel-1 GRD SAR Images and Google Earth Engine : A Case Study OF DARBHANGAH, BIHAR. *Recent Advances in Geospatial Technology & Applications, IIRS Dehradun, India*, *August*, 1–4. https://www.researchgate.net/publication/343539830

Mukherjee, R., Policelli, F., Wang, R., Tellman, B., Sharma, P., Zhang, Z., & Giezendanner, J. (2023). A globally sampled high-resolution hand-labeled validation dataset for evaluating surface water extent maps. *Earth System Science Data Discuss [Preprint],*. https://doi.org/10.5194/essd-2023-168

Nguyen, H. H., Cho, S., Jeong, J., & Choi, M. (2021). A D-vine copula quantile regression approach for soil moisture retrieval from dual polarimetric SAR Sentinel-1 over vegetated terrains. *Remote Sensing of Environment*, *255*, 112283. https://doi.org/10.1016/J.RSE.2021.112283

Nobre, A. D., Cuartas, L. A., Hodnett, M., Rennó, C. D., Rodrigues, G., Silveira, A., Waterloo, M., & Saleska, S. (2011). Height Above the Nearest Drainage - a hydrologically relevant new terrain model. *Journal of Hydrology*, *404*(1–2), 13–29. https://doi.org/10.1016/j.jhydrol.2011.03.051

Nobuyuki Otsu. (1979). A Threshold Selection Method from Gray-Level Histograms. *IEEE Trans. Syst. Man Cybern*, *9*(1), 62–66. https://ieeexplore.ieee.org/stamp/stamp.jsp?arnumber=4310076

Oneto, L., Donini, M., Luise, G., Ciliberto, C., Maurer, A., & Pontil, M. (2020). Exploiting MMD and Sinkhorn Divergences for Fair and Transferable Representation Learning. *Advances in Neural Information Processing Systems*, *33*, 15360–15370.

Rahnemoonfar, M., Chowdhury, T., Sarkar, A., Varshney, D., Yari, M., & Murphy, R. R. (2021). FloodNet: A High Resolution Aerial Imagery Dataset for Post Flood Scene Understanding. *IEEE Access*, *9*, 89644–89654. https://doi.org/10.1109/ACCESS.2021.3090981

Rennó, C. D., Nobre, A. D., Cuartas, L. A., Soares, J. V., Hodnett, M. G., Tomasella, J., & Waterloo, M. J. (2008). HAND, a new terrain descriptor using SRTM-DEM: Mapping terra-firme rainforest environments in Amazonia. *Remote Sensing of Environment*, *112*(9), 3469–3481. https://doi.org/10.1016/j.rse.2008.03.018

Ronneberger, O., Fischer, P., & Brox, T. (2015). U-net: Convolutional networks for biomedical image segmentation. *Lecture Notes in Computer Science (Including Subseries Lecture Notes in Artificial Intelligence and Lecture Notes in Bioinformatics)*, *9351*, 234–241. https://doi.org/10.1007/978-3-319-24574-4_28

Schmitt, M., Ahmadi, S. A., Xu, Y., Taskin, G., Verma, U., Sica, F., & Haensch, R. (2023). There Are No Data Like More Data: Datasets for deep learning in Earth observation. *IEEE Geoscience and Remote Sensing Magazine*. https://doi.org/10.1109/MGRS.2023.3293459

Segmentation Models, *GitHub repository*, https://github.com/qubvel/segmentation_models.pytorch, last accessed March 1, 2024.

Singh, S., & Kansal, M. L. (2022). Chamoli flash-flood mapping and evaluation with a supervised classifier and NDWI thresholding using Sentinel-2 optical data in Google earth engine. *Earth Science Informatics*, *15*(2), 1073–1086. https://doi.org/10.1007/s12145-022-00786-8

Sit, M., Demiray, B., & Demir, I. (2021a). Short-term hourly streamflow prediction with graph convolutional GRU networks. arXiv preprint arXiv:2107.07039.

Sit, M., Seo, B. C., & Demir, I. (2021b). Iowarain: A statewide rain event dataset based on weather radars and quantitative precipitation estimation. arXiv preprint arXiv:2107.03432.

Slater, L. J., Anderson, B., Buechel, M., Dadson, S., Han, S., Harrigan, S., Kelder, T., Kowal, K., Lees, T., Matthews, T., Murphy, C., & Wilby, R. L. (2021). Nonstationary weather and water extremes: A review of methods for their detection, attribution, and management. *Hydrology and Earth System Sciences*, *25*(7), 3897–3935. https://doi.org/10.5194/HESS-25-3897-2021

Tiwari, V., Kumar, V., Matin, M. A., Thapa, A., Ellenburg, W. L., Gupta, N., & Thapa, S. (2020). Flood inundation mapping-Kerala 2018; Harnessing the power of SAR, automatic threshold detection method and Google Earth Engine. *PLoS ONE*, *15*(8 August), e0237324. https://doi.org/10.1371/journal.pone.0237324

Twele, A., Cao, W., Plank, S., & Martinis, S. (2016). Sentinel-1-based flood mapping: a fully automated processing chain. *International Journal of Remote Sensing*, *37*(13), 2990–3004. https://doi.org/10.1080/01431161.2016.1192304

Wieland, M., Martinis, S., Kiefl, R., & Gstaiger, V. (2023). Semantic segmentation of water bodies in very high-resolution satellite and aerial images. *Remote Sensing of Environment*, *287*, 113452. https://doi.org/10.1016/J.RSE.2023.113452

Xiang, Z., Demir, I., Mantilla, R., & Krajewski, W. F. (2021). A regional semi-distributed streamflow model using deep learning.

Xiong, Q., Li, G., Yao, X., & Zhang, X. (2023). SAR-to-Optical Image Translation and Cloud Removal Based on Conditional Generative Adversarial Networks: Literature Survey, Taxonomy, Evaluation Indicators, Limits and Future Directions. *Remote Sensing 2023, Vol. 15, Page 1137*, *15*(4), 1137. https://doi.org/10.3390/RS15041137

Yang, Q., Shen, X., Anagnostou, E. N., Mo, C., Eggleston, J. R., & Kettner, A. J. (2021). A High-Resolution Flood Inundation Archive (2016–the Present) from Sentinel-1 SAR Imagery over CONUS. *Bulletin of the American Meteorological Society*, *102*(5), E1064–E1079. https://doi.org/10.1175/BAMS-D-19-0319.1

Yang, Z., Diao, C., & Li, B. (2021). A robust hybrid deep learning model for spatiotemporal image fusion. *Remote Sensing*, *13*(24), 5005. https://doi.org/10.3390/rs13245005

Yildirim, E., & Demir, I. (2022). Agricultural flood vulnerability assessment and risk quantification in Iowa. *Science of The Total Environment*, *826*, 154165. https://doi.org/10.1016/J.SCITOTENV.2022.154165

Zeng, Z., Gan, Y., Kettner, A. J., Yang, Q., Zeng, C., Brakenridge, G. R., & Hong, Y. (2020). Towards high resolution flood monitoring: An integrated methodology using passive microwave brightness temperatures and Sentinel synthetic aperture radar imagery. *Journal of Hydrology*, *582*, 124377. https://doi.org/10.1016/j.jhydrol.2019.124377

Zhang, W., Hu, B., & Brown, G. S. (2020). Automatic surface water mapping using polarimetric SAR data for long-term change detection. *Water (Switzerland)*, *12*(3), 872. https://doi.org/10.3390/w12030872

Zhang, Y., Liu, P., Chen, L., Xu, M., Guo, X., & Zhao, L. (2023). A new multi-source remote sensing image sample dataset with high resolution for flood area extraction: GF-FloodNet. *International Journal of Digital Earth*, *16*(1), 2522–2554. https://doi.org/10.1080/17538947.2023.2230978